Clear-sky Irradiance Model for Real-time Sky Imager Application

Julien Nou, Rémi Chauvin, Stéphane Thil, Julien Eynard, Stéphane Grieu

HAL Id: hal-01273346

https://hal-univ-perp.archives-ouvertes.fr/hal-01273346

Submitted on 5 Apr 2016

International Conference on Concentrating Solar Power and Chemical Energy Systems, SolarPACES 2014

Clear-sky irradiance model for real-time sky imager application

J. Nou[1], R. Chauvin[1,2], S. Thil[1,2], J. Eynard[1,2] and S. Grieu[1,2,*]

[1]*PROMES-CNRS, Rambla de la thermodynamique, Tecnosud, 66100 Perpignan, France*
[2]*University of Perpignan Via Domitia, 52 Avenue Paul Alduy, 66860 Perpignan, France*

Abstract

In a context of sustainable development, enthusiasm for concentrated solar power technologies is developing. So, the CSPIMP (Concentrated Solar Power efficiency IMProvement) project started in 2013 in order to achieve a better competitiveness for the CSP plants. Its main target is to develop new procedures to improve steam turbine start up cycles, maintenance activities and plant control. One challenge in the project is to better forecast the solar resource in order to optimize plants operation. The development of a clear sky model is therefore an essential step to forecast Direct Normal Irradiance (DNI) because clear sky represents the nominal operating conditions of a concentrating solar power plant. This paper focuses on estimating DNI under clear-sky conditions using a knowledge model based on the coefficient of relative optical air mass, DNI and atmospheric turbidity fluctuations. The satisfactory results obtained validate the proposed methodology.

Keywords: Clear sky irrandiance model; sky imager; real-time application; concentrating solar power systems.

1. Introduction

It is widely acknowledged by solar companies and plant operators that cost remains the main drawback of Concentrating Solar Power (CSP) systems. In that context, the CSPIMP (Concentrated Solar Power efficiency IMProvement) project has been initiated in 2013 in order to make CSP plants more competitive. The main target of the project is to improve plant efficiency by developing better procedures for steam turbine start up cycles and maintenance activities as well as proposing advanced plant control schemes.

---

* Corresponding author. Tel.: +33468682257; fax: +33468682213.
  E-mail address: stephane.grieu@promes.cnrs.fr

Depending on the CSP configuration (turbine, back-up generator, buffer tank, storage system…), a customized forecast model must be built to deal with the plant's specific behaviour against solar variability. Different forecast models exist to assess the solar resource at short-term (i.e. a few minutes), medium-term (i.e. a few hours) and long-term (i.e. a few days) horizons.

For instance, Numerical Weather Prediction (NWP) models are well adapted to the forecast of changes in meteorological parameters at long-term horizon [1]. These models are able to provide forecasts of parameters such as temperature, relative humidity and wind speed but also global and direct irradiance, which is relevant information for CSP plant strategy improvement and integration into the electricity grid. However, NWP models do not take into account the cloud cover. So, to refine their spatial and temporal resolutions, such models can be coupled with satellite imagery. Indeed, satellite imagery is able to provide more comprehensive information about cloud motion [2]. Images are provided every 15 minutes by geostationary satellites, as Meteosat in Europe or GEOS in the USA, with a spatial resolution of ~1 km². From these images, it is possible to obtain a daily trend of solar irradiance, what can be relevant in order to optimize the use of a storage system. Moreover, NWP models and satellite imagery can be combined with time series forecasting models, based on a historical climate database, with the aim of identifying cycles and/or trends in the solar resource [3]. However, NWP models, even coupled with satellite imagery, are not suited to the real-time management of a solar power plant.

Images can also be provided by ground-based cameras, named sky imagers. Such cameras allow solar radiation to be forecasted at high spatial (~100 m²) and temporal (< 30 min) resolutions. Indeed, sky imagers can provide in real-time a very short term forecast of the beam attenuation produced by clouds, allowing the power plant owner to make more accurate bids in the market with less risk of under-generation (leading to penalties) or over-generation (leading to losses due to curtailment). Sky imagers can also contribute to an increase in equipment lifetime and reliability using forecasting algorithms developed to take advantage of solar variability. It is especially interesting for storage systems for which the overall return on investment is directly related to the system's lifetime. A smart charging and release algorithm can take advantage of the future availability and variability of the solar resource to better coordinate the backup generator with a buffer tank. It could help to reduce the number of charging/release cycles and would make storage systems more economically feasible. Finally, sky-imaging systems can also be used to adjust the Heat Transfer Fluid (HTF) flow in real time. At the moment, CSP plants are working with strong limitations on the HTF flow in order to avoid bending absorber pipes during fast fluctuations of the solar resource. Having the HTF flow as a function of the DNI and using a sky-imaging system would allow the plant to operate with lower limitations on this flow. Consequently, HTF temperature would be more often at its nominal point, allowing the plant to be more effective.

Among the different approaches and devices available to perform the forecasting of solar resource, we focused on ground-based cameras which are well-suited to estimate and forecast the clearness index at a very short-term horizon and a high spatial resolution [4–6]. Usually, this forecasting approach consists in two complementary steps. The first one is about determining the clearness index (its value ranges between 0 and 1) corresponding to the sun occultation caused by clouds. The second step is related to the clear sky model used to estimate the theoretical solar irradiance received at ground level without clouds. Developing a clear sky model is therefore an essential step to forecast direct normal irradiance. Nowadays, clear sky models developed for satellite imagery [2,7] or ground-based camera applications [4–6] are often inappropriate to real-time applications. Indeed, at the moment, there are no works dealing with the clear sky detection in real-time. As an example, in a previous work [8], we proposed a methodology based on a multi-resolution analysis (using the discrete wavelet transform) in order to detect clear sky days in our database. This approach is useful for data preprocessing and model development but not adapted to real-time applications like solar power plants management. Moreover, the existing models dealing with clear sky irradiance are relatively basic. For instance, an approach is proposed to obtain short-term forecasts of DNI at the ground level by authors assuming that DNI is constant (900 W.m^{-2}) during the considered period (from 10:00 PM to 14 PM) [6]. More often, clear sky irradiance models use yearly or monthly atmospheric turbidity values or are based on polynomials. In their work [4], Quesada-Ruiz *et al.* computed clear-sky DNI from an eighth-order polynomial of the cosine of the solar zenith angle using a Least Squares Method (LSM). However, the results they obtained show that, for clear sky conditions, the model is less effective than a basic persistent model. In another study, clear sky irradiance is computed from the Linke turbidity coefficient. This coefficient has the main drawback to be dependent on air mass [5]. In order to overcome these different problems, a knowledge model based on the coefficient of relative optical air mass, DNI and atmospheric turbidity fluctuations is proposed in order to estimate the clear sky

DNI in real time. The paper is organized as follows: section 2 is about the PROMES-CNRS experimental platform as well as the measured and computed variables used in the clear sky model development and validation. Section 3 focuses first on atmospheric turbidity. In addition, the model development and optimization processes are described. Section 4 deals with the estimation results we obtained and an overall analysis. The paper ends with a conclusion and outlook on further work.

Nomenclature	
b	Multiplicative coefficient based on the altitude of a considered site
i	Position of an element in a given vector
k_{rand}	Sequence of pseudo random values drawn from the standard distribution on [0,1]
k_t	Clearness index
m	Altitude-corrected air mass
r	Sun-Earth distance correction factor
t_{past}	Last time atmospheric turbidity is trustworthy
u	Binary sequence resulting from the visual highlight of clear sky instants
v	Pseudo Random Binary Sequence (PRBS)
v'	Sequence of pseudo random values drawn from the standard distribution on [0,1]
w	Sequence obtained by multiplying the sequences u and v term by term
C_1	Model constant 1
C_2	Model constant 2
C_T	Coefficient of atmospheric turbidity
I	Direct normal irradiance (W.m^{-2})
I_0	Extra-terrestrial solar irradiance (W.m^{-2})
I_{CS}	Broadband direct normal irradiance under clear sky conditions (W.m^{-2})
I_G	Generated solar irradiance sequence (W.m^{-2})
N	Total number of elements in a given vector
$R_{0/1}$	Degradation ratio dealing with the proportion of "1" in sequence v
T	Atmospheric transmittance resulting from both scattering and absorption of the sunlight
T_{LI}	Atmospheric turbidity (Ineichen and Perez [9])
Δt	Elapsed time since the last trustworthy atmospheric turbidity measurement (s)
Δt_{max}	Maximum value of Δt (s)
Δt_{min}	Minimum value of Δt (s)
ΔT	Measured change in atmospheric turbidity
ΔT_{lim}	Threshold of atmospheric turbidity change
ΔT_{max}	Maximum accepted change in atmospheric turbidity
ΔT_{min}	Minimum accepted change in atmospheric turbidity

2. Experimental set-up and database

(a) Experimental platform   (b) PROMES sky imager   (c) Irradiance sensor (RSI)

Fig. 1. View of the experimental platform.

To develop and validate our model, an experimental platform (Fig. 1.a) has been installed at the PROMES-CNRS laboratory in 2013 (Perpignan, France, latitude is 42.66° N, longitude is 2.91° E and elevation is ~50 m). This part of the paper provides a hardware overview of the platform and specifies the working conditions of the different instruments used.

2.1. PROMES Sky Imager

To determine the clear sky index (its value ranges between 0 and 1) corresponding to the sun occultation caused by clouds, the PROMES-CNRS laboratory has decided to build its own system, fully customizable from both a hardware and software point of view. This decision has been motivated by the fact that all the existing sky imagers suffer from drawbacks and PROMES-CNRS believes that a customizable solution would make such systems more attractive. After a detailed review of the different cameras proposed by manufacturers, a 5-megapixel camera with a color CMOS sensor has finally been selected. The camera, named 5481VSE-C and provided by IDS, is equipped with a Fujinon fisheye lens and protected by a waterproof enclosure manufactured by autoVimation (Fig. 1.b). Images are collected every 20 seconds at a resolution of 1920 x 2560 pixels and with a bit depth of 8 bits per channel (i.e. 3x8 bits).

2.2. Irradiance sensor

A Rotating Shadowband Irradiometer (RSI) (Fig. 1.c) has been installed next to the sky imager in order to measure every minute, with a good precision, the solar irradiance components. Equipped with a silicon photodiode radiometer and a shadow band, this instrument allows Direct Normal Irradiance (DNI), Global Horizontal Irradiance (GHI) and Diffuse Horizontal Irradiance (DHI) to be measured or deduced from measurements. The data are collected by the sky imager software and immediately included in the process analysis. In the present study, we only focus on DNI measurement because it is a key point in the clear sky model development and because in the CSP technology, the power production is only affected by the direct component.

2.3. Database

The database used to develop and validate the clear sky model is composed of data collected by the experimental platform and data derived from the sun-earth equations given by the SG2 algorithm [10]. Knowing the Julian date and the localization of the considered site (latitude, longitude, and altitude), this algorithm is able to give quickly and with high accuracy all information like air mass, azimuth/zenith angles, and extraterrestrial solar radiation. In order to avoid missing data, we considered measures from February the 5th to March the 21st, 2014.

3. Clear-sky irradiance model

Clear sky is the nominal operating conditions of a solar power plant. Consequently, the clear sky irradiance model is a key component in a forecasting approach. This section of the paper deals with the model developed by the PROMES-CNRS laboratory for our real-time sky imager application. So, a knowledge model based on the coefficient of relative optical air mass, DNI and atmospheric turbidity fluctuations is proposed in order to estimate the clear sky DNI in real time (I_{CS}). Before addressing the development phase, let's talk about atmospheric turbidity.

3.1. Atmospheric turbidity

Under clear sky conditions, the broadband DNI (I_{CS}) is given by (1):

$$I_{CS} = r \cdot I_0 \cdot T \tag{1}$$

with I_0 the extraterrestrial solar irradiance ($I_0 = 1361.2$ W.m^{-2} [11]), r the sun-earth distance correction factor and T the atmospheric transmittance resulting from both scattering and absorption of the sunlight. This atmospheric transmittance can be obtained using radiation transfer models [12] or a broadband turbidity coefficient like the well-

known Linke turbidity coefficient [13]. Although radiation transfer models have proven to be able to forecast clear sky DNI with unsurpassed accuracy, they require Aerosol Optical Depth (AOD) data which are difficult to measure or rarely available with high accuracy. On the other hand, models based on a broadband turbidity coefficient give a lower accuracy than radiation transfer models but can be easily implemented because they only derive from broadband beam radiation measurement networks. In 2002, Ineichen and Perez [9] proposed an empirical formulation of the turbidity coefficient for the normal beam clear sky radiation including both scattering and absorption phenomena. This new formulation is less dependent on air mass than the Linke turbidity coefficient. Because this coefficient (T_{LI}) is well adapted for on-site and real-time applications, it has been selected as a starting point in the development of our clear sky model. It is calculated using equation (2):

$$T_{LI} = 1 + \left[\frac{11.1}{m} \cdot \ln \left(\frac{bI_0}{I_{CS}} \right) \right]$$

(2)

with m the optical air mass and b a coefficient taking into account the altitude of the considered site.

3.2. Real-time estimation of the atmospheric turbidity

During the real-time DNI acquisition process, each new DNI value I must be classified as clear sky irradiance or not. It is a key information because it allows the clearness index k_t to be calculated. It is defined as follows (3):

$$k_t = \frac{I}{I_{CS}}$$

(3)

with I the measured irradiance and I_{CS} the estimated clear sky irradiance. This index is a powerful indicator of the beam attenuation produced by clouds and is frequently used in solar resource forecasting [4–6]. To classify the last measured DNI value correctly, an algorithm based on the atmospheric turbidity transient behaviour has been developed. It takes advantage of the fact that atmospheric turbidity fluctuations are low through the day. The algorithm works as follows (Fig. 2):
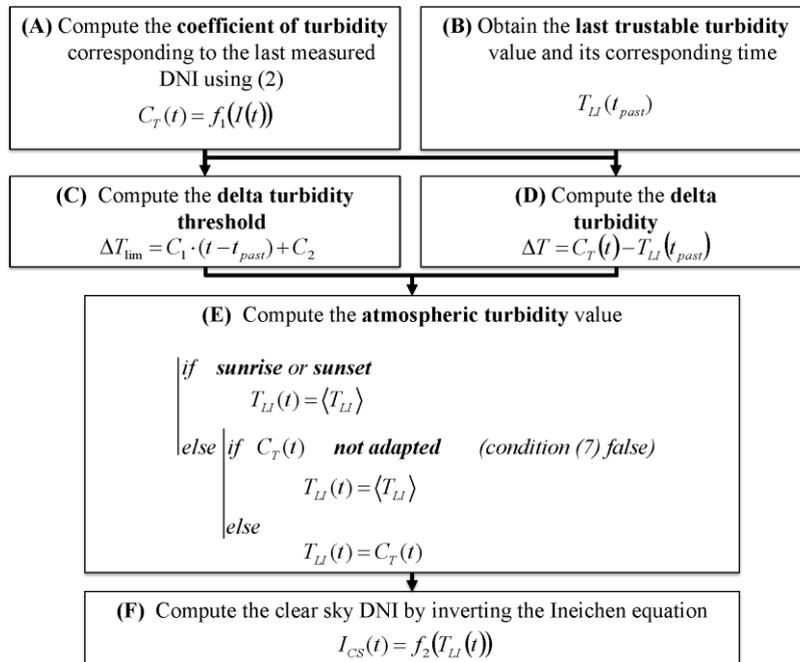

(A) Compute the **coefficient of turbidity** corresponding to the last measured DNI using (2)
$$C_T(t) = f_1(I(t))$$

(B) Obtain the **last trustable turbidity** value and its corresponding time
$$T_{LI}(t_{past})$$

(C) Compute the **delta turbidity threshold**
$$\Delta T_{lim} = C_1 \cdot (t - t_{past}) + C_2$$

(D) Compute the **delta turbidity**
$$\Delta T = C_T(t) - T_{LI}(t_{past})$$

(E) Compute the **atmospheric turbidity** value

if **sunrise** or **sunset**
$$T_{LI}(t) = \langle T_{LI} \rangle$$

else if $C_T(t)$ **not adapted** (condition (7) false)
$$T_{LI}(t) = \langle T_{LI} \rangle$$

else
$$T_{LI}(t) = C_T(t)$$

(F) Compute the clear sky DNI by inverting the Ineichen equation
$$I_{CS}(t) = f_2(T_{LI}(t))$$

Fig. 2. Diagram of the developed knowledge model.

Each time DNI $\left(I(t)\right)$ is measured (under clear sky conditions or not), a corresponding coefficient related to atmospheric turbidity $C_T(t)$ is calculated **(A)** using equation (2). This coefficient $C_T(t)$ is equal to atmospheric turbidity $T_{LI}(t)$ only if the measured DNI $\left(I(t)\right)$ corresponds to the clear sky DNI $\left(I_{CS}(t)\right)$. So, in order to decide if $C_T(t)$ corresponds or not to atmospheric turbidity, changes in atmospheric turbidity are considered via its maximum plausible change ΔT_{lim} **(C)** and its measured change ΔT **(D)**. These two variables are computed from the last time (t_{past}) atmospheric turbidity T_{LI} is trustworthy **(B)**. So, t_{past} is the last time the coefficient related to atmospheric turbidity $C_T(t)$ is used as atmospheric turbidity. The threshold ΔT_{lim} has been computed on the basis of the transient atmospheric turbidity behaviour we highlighted in our database. Indeed, the bigger Δt is, the more plausible the atmospheric turbidity increase is. However, according to its daily behaviour (atmospheric turbidity never increases all the day), a maximum change is defined. Fig. 3 shows how ΔT_{lim} has been computed according to Δt.
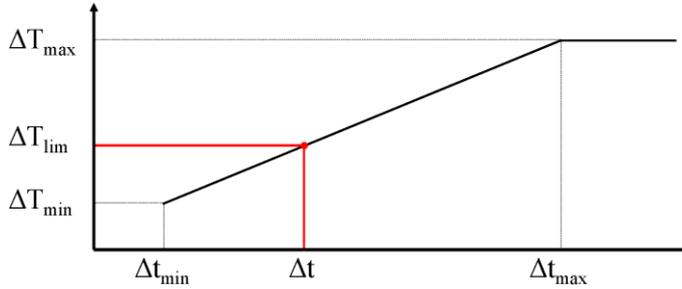

Fig. 3. ΔT_{lim} vs. Δt.

For now, a simple linear interpolation has been performed in order to determine ΔT_{lim}. Therefore, ΔT_{lim} is given by equation (4), with C_1 and C_2 the slope and the intercept of the curve (between Δt_{min} and Δt_{max}), respectively (5):

$$\Delta T_{lim} = \min(C_1 . \Delta t + C_2 , \Delta T_{max}) \tag{4}$$

$$C_1 = (\Delta T_{max} - \Delta T_{min})/(\Delta t_{max} - \Delta t_{min}) \text{ and } C_2 = \Delta T_{min} - \Delta t_{min} \cdot C_1 \tag{5}$$

Δt_{min} and ΔT_{min} mean that atmospheric turbidity cannot increase more than ΔT_{min} for two consecutive DNI acquisitions Δt_{min} ($\Delta t_{min} = 20$ seconds and $\Delta T_{min} = 0.045$). Δt_{max} and ΔT_{max} mean that atmospheric turbidity cannot increase more than 1 through the day ($\Delta t_{max} = 10$ hours and $\Delta T_{max} = 1$). These four parameters have been set taking into account the acquisition time step, accuracy in RSI measurements as well as changes in atmospheric turbidity one can observe in the database. As a result, they are proper to both the considered site and measurement devices used. ΔT is about the measured change in atmospheric turbidity. It is computed as follows (6):

$$\Delta T = C_T(t) - T_{LI}\left(t_{past}\right) \tag{6}$$

Once these two thresholds are computed (ΔT_{lim} and ΔT), a decision based on their comparison is taken **(E)** in order to determine if the computed coefficient $C_T(t)$ is, or not, the "real" atmospheric turbidity $T_{LI}(t)$. This decision is taken according to the following conditions (7):

$$\Delta T > \Delta T_{lim} \text{ or } C_T < T_{min} \text{ or } C_T > T_{max} \tag{7}$$

where T_{min} and T_{max} are constants defined empirically (using our database) and derived from the minimum and maximum possible values of atmospheric turbidity. If (7) is true (i.e. C_T is not plausible), the mean atmospheric turbidity value $\langle T_{LI} \rangle$ calculated over the last five minutes is assigned to $T_{LI}(t)$. However, the time of the day impacts the decision process. For example, during sunrise or sunset, $\langle T_{LI} \rangle$ is consistently used because atmospheric turbidity is not easy to compute in such periods. This approach provides more stable values. Sunrise and sunset have been determined from both the air mass m and time, as shown in Table 1. Finally, once atmospheric turbidity $\left(T_{LI}(t)\right)$ is computed, the clear sky DNI $\left(I_{CS}(t)\right)$ is obtained **(F)** by inverting equation (2).

Table 1. Sunrise and sunset determining.

Sunrise	Sunset
$m > 10$ and *time* $< 12:00$ p.m.	$m > 6$ and *time* $> 12:00$ p.m.

3.3. Model evaluation

In order to validate our model, an evaluation methodology has been defined. This methodology is based on the different steps presented by Fig. 4. The main target is to quantify model accuracy. The idea is then to generate a signal similar to DNI and a noise is added to simulate variations caused by clouds. This noise is only added during some clear sky instants in order to use clear sky DNI measurements as reference during the validation step. The next section of the paper gives more details about this process.
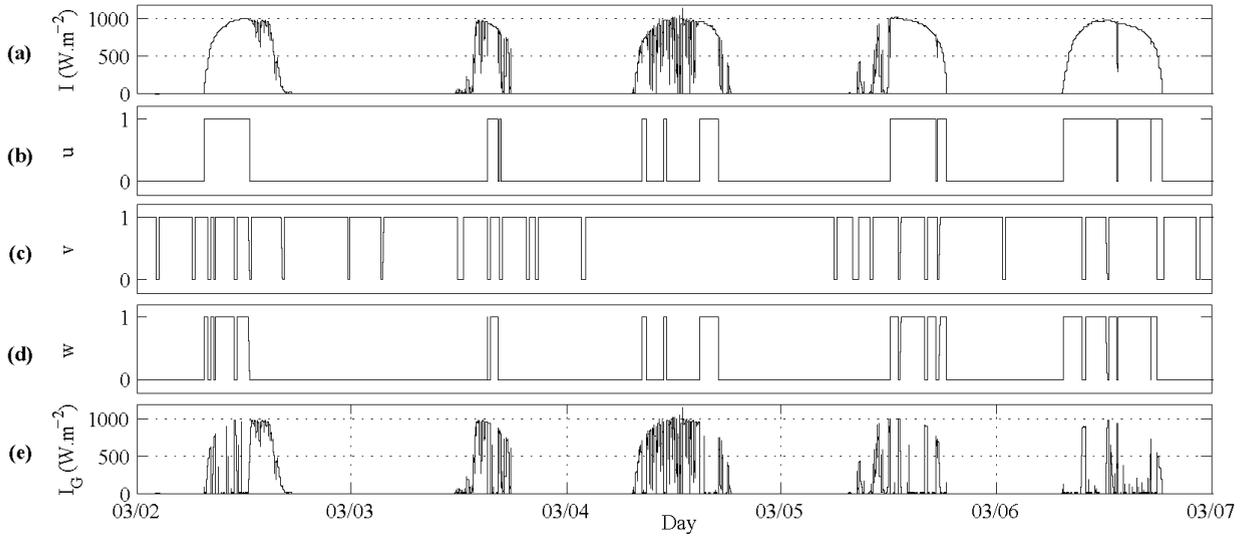

Fig. 4. Overview of the five steps used for model evaluation.

From the measured DNI (I) and thanks to pictures taken by our sky imager (in order to be sure that the sun disk appears clearly), clear sky instants have been visually highlighted **(a)**. u is the resulting signal **(b)**. It is a binary sequence where 0 corresponds to a sun occulted by clouds while 1 is about clear sky. On Fig. 4, only five consecutive days are plotted. However, our study considers 45 days of the database, which is about 150 hours of clear sky data. In order to evaluate our clear sky model, we degraded a part of these 150 hours of data **(c)**. Considering this noisy signal, we compared the clear sky values given by our model and measured clear sky data (without noise). Firstly, we generated a random sequence denoted v' (in which each element $v'_i \in [0,1]$). From v' we generated v, the Pseudo Random Binary Sequence (PRBS), by using (8), according to the ratio $R_{0/1}$ dealing with the proportion of "1" in such a sequence:

$$
\begin{aligned}
&\text{if } v_i' > R_{0/1} \\
&\quad \text{then } v_i = 0 \\
&\quad \text{else } v_i = 1
\end{aligned}
\tag{8}
$$

In our study, this ratio ranges between 0.1 and 0.9 (because it can be very different, depending on the season of the year). As a consequence, the initial signal I has been degraded according to $R_{0/1}$. For instance, a ratio $R_{0/1}$ equal to 0.7 means that the initial clear sky DNI signal is degraded by 70 %. Then, multiplying the sequences u and v term by term, we obtained the sequence w **(d)**. This sequence was determined by using the following expression (9):

$$
w_{1 \leq i \leq N} = (u_i \times v_i)_{1 \leq i \leq N}
\tag{9}
$$

where i is about the position of an element in a given vector and N is the total number of elements in that vector. Finally, from this signal, we generated another signal I_G, used as input of our model **(e)**. It is defined as follows: when w is equal to 0, $I_G = I$ and when w is equal to 1, $I_G = I \times k_{rand}$. k_{rand} is a sequence of pseudo random values drawn from the standard distribution on the interval $[0,1]$. From this methodology, it is possible to test our model and evaluate its efficiency knowing the real values of the clear sky DNI (when $u_i = 1$, with $1 \leq i \leq N$). In order to quantify the model accuracy, we considered both the Mean Absolute Error (MAE) and the Normalized Root-Mean-Square Error (NRMSE), defined as follows (10):

$$MAE = \frac{1}{n}\sum\left|I_{CS} - \hat{I}_{CS}\right| \qquad NRMSE = 100 \times \frac{\sqrt{\frac{1}{n}\Sigma(I_{CS} - \hat{I}_{CS})^2}}{I_{CS_{max}} - I_{CS_{min}}} \qquad (10)$$

with $I_{CS_{min}}$, $I_{CS_{max}}$, I_{CS} and $\hat{I}_{CS}$ the minimum, maximum, measured and estimated values of the clear sky DNI, respectively. The results we obtained using the proposed knowledge-based model are presented in the following section of the paper (section 4).

4. Results and discussion

Using our knowledge model and the noisy signal I_G, one can obtain clear sky DNI values. To obtain more relevant and reliable results, we generated ten times the pseudo random binary sequence w. The impact of $R_{0/1}$ on both the MAE and NRMSE is highlighted by Table 2.

Table 2. Impact of $R_{0/1}$ on both the MAE and NRMSE.

$R_{0/1}$	0.1	0.2	0.3	0.4	0.5	0.6	0.7	0.8	0.9
MAE (W.m^{-2})	16.1	17.5	19.2	20.3	21.4	22.7	24.6	27.2	33.4
STD MAE (W.m^{-2})	4.77	4.68	3.44	2.95	3.05	2.84	1.83	1.90	2.46
NRMSE (%)	1.01	1.26	1.56	1.63	1.72	1.79	1.90	2.14	2.77
STD NRMSE (%)	0.63	0.82	0.65	0.58	0.58	0.50	0.35	0.31	0.32

Taking a look at this table, one can notice that the more the ratio $R_{0/1}$ increases (i.e. the higher the degradation of the signal) the quicker the MAE and NRMSE increase. Indeed, considering a high degradation, clear sky data are less available to facilitate a good computation of atmospheric turbidity and, therefore, the clear sky DNI. With a ratio $R_{0/1}$ set to 0.1, the MAE and NRMSE are 16.1 W.m^{-2} and 1.01%, respectively. With a ratio $R_{0/1}$ set to 0.9, the MAE and NRMSE are 33.4 W.m^{-2} and 2.77%, respectively. Moreover, we clearly notice that the results are very dependent on the operating conditions considered for model evaluation ($R_{0/1}$ values). According to the DNI measurements realized for this study, the mean ratio of clear sky data during a day is close to 32 %. This corresponds to a ratio $R_{0/1}$ equal to 0.68. So, the results obtained for the on-site measured ratio ($R_{0/1} = 0.7$) are satisfactory because of a MAE equal to 24.6 W.m^{-2} and a NRMSE equal to 1.9% (Table 2). Fig. 5 presents the results obtained using the proposed clear sky model for three consecutive days of March 2014. These three days have been selected in order to highlight how the model is able to work with different DNI behaviours. $R_{0/1}$ has been set to 0.7 in order to be representative of on-site measurements.

The three selected days (March 1 to March 3) have different solar irradiance profiles. For each day, we can note sharp and frequent changes in DNI (i.e. cloudy periods of limited duration) and periods during which DNI is insignificant (overcast). Indeed, when the coefficient related to atmospheric turbidity $\left(C_T(t)\right)$ does not correspond to atmospheric turbidity (i.e. condition (7) is true), the mean value of atmospheric turbidity is used (if it is not available during the last five minutes, like during sunrise, the last value of the day before is used). However, when $C_T(t)$ can be considered as equal to atmospheric turbidity (i.e. condition (7) is false), the values of $T_{LI}(t)$ are updated. These updates produce more or less important changes in the red curve, depending on the time between two measurements or the magnitude of the update.

Generally, the clear sky DNI values given by the model form an upper limit envelope (the red curve on Fig. 5) and clear sky DNI fluctuations, caused by the atmospheric turbidity updates, are relatively slight. It was a key point

to obtain slight fluctuations on clear sky DNI estimation in order to avoid problems during the short-term DNI forecasting process. Indeed, as previously explained, the development of a reliable and accurate clear sky model is an essential step in solar resource forecasting. Thus, the more reliable the forecast is, the more efficient the real-time management of a solar power plant will be.
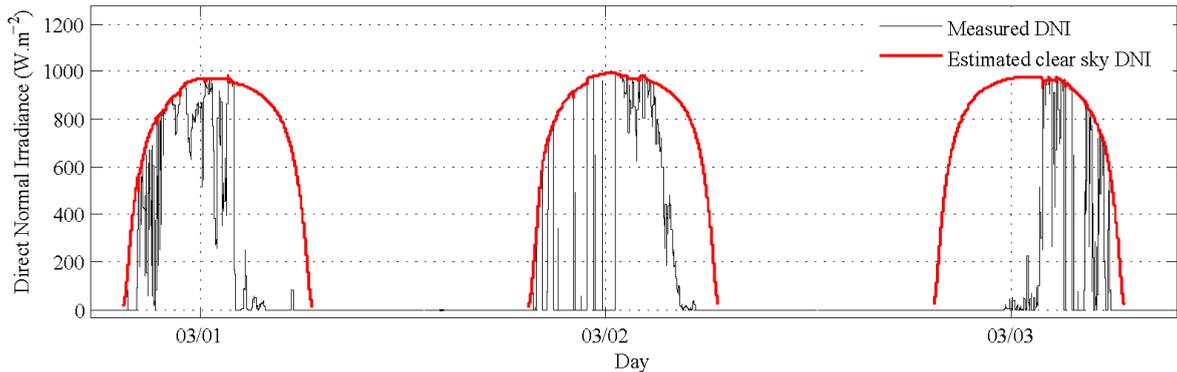

Fig. 5. Measured clear sky DNI and clear sky DNI estimated by the model, with $R_{0/1}$ set to 0.7.

5. Conclusion and outlook

The CSPIMP (Concentrated Solar Power efficiency IMProvement) project started in 2013 in order to achieve a better competitiveness for the CSP plants. One challenge in the project is to improve forecast of the solar resource in order to optimize plants operation. The development of a clear sky model is therefore an essential step to forecast Direct Normal Irradiance (DNI) because clear sky represents the nominal operating conditions of a concentrating solar power plant. So, this paper focuses on estimating DNI under clear-sky conditions using a knowledge model based on the coefficient of relative optical air mass, DNI and atmospheric turbidity fluctuations. This model takes advantage of the lower variability of atmospheric turbidity, in comparison to the DNI variability.

The empirical formulation of atmospheric turbidity proposed by Ineichen and Perez has been selected in this study because it proved to be less dependent on air mass than the widely-used Linke turbidity coefficient; it is also well adapted for on-site and real-time applications. A validation procedure has been proposed and allowed the model accuracy to be highlighted. With a ratio $R_{0/1}$ equal to 0.7 (see section 3.3), the MAE and NRMSE are 25 W.m^{-2} and 2 %, respectively. In addition, the structure of the proposed knowledge-based model makes it well adapted to real-time applications. As a result, it will be soon implemented and validated on site (Palma del Rio CSP plant, Spain).

Future work will focus on evaluating the error distribution in the course of the day (error vs. air mass) as well as new options to deal with $C_T(t)$ (i.e. the coefficient related to atmospheric turbidity) not corresponding to atmospheric turbidity. Finally, in order to forecast at short-term horizon the clear sky DNI and then DNI for all types of sky conditions, a persistent model based on atmospheric turbidity will be developed and evaluated. For such a forecast horizon, this approach has proven to be adequate, due to the low variability of atmospheric turbidity.

References

[1]   Lara-Fanego V, Ruiz-Arias JA, Pozo-Vázquez D, Santos-Alamillos FJ, Tovar-Pescador J. Evaluation of the WRF model solar irradiance forecasts in Andalusia (southern Spain). Solar Energy 2012;86:2200–17. doi:10.1016/j.solener.2011.02.014.
[2]   Mefti A, Adane A, Bouroubi MY. Satellite approach based on cloud cover classification: Estimation of hourly global solar radiation from meteosat images. Energy Conversion and Management 2008;49:652–9. doi:10.1016/j.enconman.2007.07.041.
[3]   Reikard G. Predicting solar radiation at high resolutions: A comparison of time series forecasts. Solar Energy 2009;83:342–9. doi:10.1016/j.solener.2008.08.007.
[4]   Quesada-Ruiz S, Chu Y, Tovar-Pescador J, Pedro HTC, Coimbra CFM. Cloud-tracking methodology for intra-hour DNI forecasting. Solar Energy 2014;102:267–75. doi:10.1016/j.solener.2014.01.030.
[5]   Chow CW, Urquhart B, Lave M, Dominguez A, Kleissl J, Shields J, et al. Intra-hour forecasting with a total sky imager at the UC San Diego solar energy testbed. Solar Energy 2011;85:2881–93. doi:10.1016/j.solener.2011.08.025.
[6]   Marquez R, Coimbra CFM. Intra-hour DNI forecasting based on cloud tracking image analysis. Solar Energy 2013;91:327–36. doi:10.1016/j.solener.2012.09.018.

[7] Perez R, Kivalov S, Schlemmer J, Hemker Jr K, Renné D, Hoff TE. Validation of short and medium term operational solar radiation forecasts in the US. Solar Energy 2010;84:2161–72. doi:10.1016/j.solener.2010.08.014.

[8] Nou J, Chauvin R, Traoré a., Thil S, Grieu S. Atmospheric Turbidity Forecasting using Side-by-side ANFIS. Energy Procedia 2014;49:2387–97. doi:10.1016/j.egypro.2014.03.253.

[9] Ineichen P, Perez R. A new airmass independent formulation for the Linke turbidity coefficient. Solar Energy 2002;73:151–7. doi:10.1016/S0038-092X(02)00045-2.

[10] Blanc P, Wald L. The SG2 algorithm for a fast and accurate computation of the position of the Sun for multi-decadal time period. Solar Energy 2012;86:3072–83. doi:10.1016/j.solener.2012.07.018.

[11] Gueymard C. An Introduction To Solar Radiation. Encyclopedia of Sustainability Science and Technology 2012.

[12] Gueymard CA. REST2: High-performance solar radiation model for cloudless-sky irradiance, illuminance, and photosynthetically active radiation – Validation with a benchmark dataset. Solar Energy 2008;82:272–85. doi:10.1016/j.solener.2007.04.008.

[13] Kasten F. The linke turbidity factor based on improved values of the integral Rayleigh optical thickness. Solar Energy 1996;56:239–44. doi:10.1016/0038-092X(95)00114-7.